

Zonal variations in the Southern Ocean heat budget

Veronica Tamsitt*

Scripps Institution of Oceanography, La Jolla, California, USA.

Lynne D. Talley

Matthew R. Mazloff

Ivana Cerovečki

*Corresponding author address: Climate, Atmospheric Science and Physical Oceanography,

Scripps Institution of Oceanography, UC San Diego, 9500 Gilman Dr., La Jolla, CA 92093-0230.

E-mail: vtamsitt@ucsd.edu

ABSTRACT

10 The three-dimensional structure of the upper ocean heat budget in the
11 Antarctic Circumpolar Current (ACC) is investigated using the $1/6^\circ$, data-
12 assimilating Southern Ocean State Estimate (SOSE) for 2005-2010. Air-sea
13 heat flux from reanalyses and SOSE show a largely unexamined zonally asym-
14 metric pattern of ocean heat gain in the Indian and Atlantic sectors and ocean
15 heat loss in the Pacific sector of the ACC. In the Atlantic and Indian sec-
16 tors of the ACC, the surface ocean heat gain is primarily balanced by cooling
17 by divergence of equatorward Ekman temperature transport driven by west-
18 erly winds. In the Pacific sector, surface ocean heat loss and cooling due to
19 divergence of Ekman temperature transport are balanced by warming by di-
20 vergence of geostrophic temperature transport, and a comparison shows this is
21 similar to the dominant heat balance found in the subtropical Agulhas Return
22 Current. Divergence of horizontal and vertical eddy advection of temperature
23 are important for warming the upper ocean in localized regions downstream
24 of major topographic features, while the mean divergence of vertical tem-
25 perature advection is generally a weak cooling term. Our results show that
26 topographic steering and zonal asymmetry in air-sea exchange lead to sub-
27 stantial zonal asymmetries in the upper ocean heat budget which are masked
28 in the zonally-averaged picture. Determining how ocean dynamics affect spa-
29 tial patterns of surface heat fluxes is a key step to understanding the upper cell
30 of the overturning circulation and the response of the overturning to future
31 changes in buoyancy forcing.

³² **1. Introduction**

³³ The Southern Ocean component of the global meridional overturning circulation is fundamen-
³⁴ tally important to climate through air-sea exchange and redistribution of heat, freshwater, carbon
³⁵ and nutrients (e.g. Sarmiento et al. 2004; Ito et al. 2010). Westerly winds drive the eastward flow-
³⁶ ing Antarctic Circumpolar Current (ACC), linking the major ocean basins and allowing inter-basin
³⁷ exchange of properties. The circumpolar nature of the Southern Ocean and predominately zonal
³⁸ flow of the ACC have led to frequent use of zonally-averaged theories to describe the Southern
³⁹ Ocean overturning circulation. Residual-mean theories explain the circumpolar-mean overturning
⁴⁰ circulation as a balance between the northward Eulerian transport driven by wind forcing and an
⁴¹ opposing southward eddy-driven transport (e.g. Karsten and Marshall 2002; Marshall and Radko
⁴² 2003). However, a zonally averaged view of the Southern Ocean is limited because interaction
⁴³ of the flow with topography and asymmetries in air-sea exchange lead to zonal asymmetries in
⁴⁴ Southern Ocean dynamics and properties, including zonal geostrophic heat transport (Sun and
⁴⁵ Watts 2002), eddy kinetic energy (Chelton et al. 1990), response of the mixed layer depth to wind
⁴⁶ variability (Sallée et al. 2010) and cross-front particle exchange (Thompson and Sallee 2012).

⁴⁷ The isopycnals in the ACC are steeply tilted upward toward Antarctica and outcrop at the surface
⁴⁸ allowing upwelling of deep water which influences air-sea exchange. Surface buoyancy gain over
⁴⁹ the Southern Ocean is necessary to convert these dense, upwelled water masses to lighter water
⁵⁰ masses at the surface and is important for setting the strength of the upper cell of the meridional
⁵¹ overturning circulation (Radko and Marshall 2006; Morrison et al. 2011). While the freshwater
⁵² flux component dominates surface buoyancy flux in polar latitudes close to Antarctica, within and
⁵³ north of the ACC heat flux component tends to dominate the surface buoyancy flux and show
⁵⁴ stronger spatial inhomogeneity and thus have a greater impact on the overturning circulation in

these latitudes (Speer et al. 2000; Iudicone et al. 2008; Cerovečki et al. 2013). However, characterization of air-sea flux has been severely limited due to a lack of direct observations (Bourassa et al. 2013) and air-sea heat fluxes have been identified as the largest contributor to uncertainty in the upper ocean heat budget (Dong et al. 2007; Faure et al. 2011). Recently developed air-sea flux products which constrain the heat fluxes with additional data sources and reduce the global long-term surface heat imbalance (Large and Yeager 2009) as well as adjusted fluxes from state estimates constrained to observations (Fig. 1a,b) show agreement in large-scale patterns of air-sea heat fluxes in the Southern Ocean (Cerovečki et al. 2011). These improved heat flux products reveal a robust, large-scale zonally asymmetric pattern in the ACC of broad ocean heat gain in the Indian and Atlantic basins and a broad region of ocean cooling in the Pacific basin (Fig. 1b). The impact of this dipole on the overturning circulation has been explored in an idealized model (Radko and Marshall 2006), finding an increase in the strength of the residual overturning circulation in the region of larger buoyancy gain in the Indian and Atlantic sectors relative to the Pacific sector and a downstream variation in the thermocline depth and stratification which is supported by observations (Sun and Watts 2002).

Dong et al. (2007) used observations and a simple model to estimate the mixed layer heat budget in the Southern Ocean from 40°S to 60°S and inferred that in the domain-average and in each basin that the dominant mixed layer balance is between air-sea heat gain and cooling by meridional Ekman advection of temperature, and that geostrophic advection of temperature plays a minimal role. This differs significantly from western boundary current regions, where poleward geostrophic advection of warm subtropical water is important in balancing ocean heat loss to the atmosphere in the mixed layer (Vivier et al. 2002; Dong and Kelly 2004; Roemmich et al. 2005). Quasi-northward Ekman transport has been identified as the dominant cooling mechanism in the ACC upper ocean and is important for Subantarctic Mode Water formation (Sloyan and Rintoul

79 2001; Rintoul and England 2002; Sallée et al. 2006, 2008). Recent work has suggested significant
80 differences in the mixed layer heat balance in different zones north, south and within the ACC
81 fronts (Sallée et al. 2008; Faure et al. 2011), and shown that regional heat balances depart from
82 the zero-order balance between air-sea flux and Ekman heat transport, highlighting the importance
83 of topography and mesoscale processes on the evolution of upper ocean temperature (Sallée et al.
84 2008; Vivier et al. 2009). Lateral eddy heat diffusion has been shown to contribute to substan-
85 tial warming locally and is strongest downstream of major topographic features but vanishes with
86 large-scale averaging (Sallée et al. 2008). Seasonal variability in the mixed layer heat budget is
87 dominated by strong seasonal variability in the air-sea heat flux (Dong et al. 2007; Sallée et al.
88 2006) although Ekman temperature advection also shows seasonal variability (Dong et al. 2007).
89 Temperature tendency variance in the ACC mixed layer has been shown to be dominated by lateral
90 advection, including both higher frequency transient eddies and lower frequency meanders (Vivier
91 et al. 2009).

92 Previous observation-based heat budget calculations use simple mixed layer models that ne-
93 glect important vertical physics due to a lack of sufficient subsurface observations (Vivier et al.
94 2009) and cannot completely close the heat budget primarily due to uncertainties in the air-sea
95 flux datasets (Dong et al. 2007). The detailed spatial variability of the heat budget in the Southern
96 Ocean is mostly unknown, particularly how the budget differs between regions with net air-sea
97 heat gain and regions of air-sea heat loss. Eddy heat fluxes have been shown to be important in
98 regions of the ACC (Sallée et al. 2006, e.g.) but limited observations have made it difficult to di-
99 agnose the eddy term in the heat budget equation. Increased model resolution and improvement of
100 ocean data assimilation techniques have prompted the development of eddy-permitting, multi-year
101 state estimates of the ocean (e.g. Mazloff et al. 2010; Wunsch and Heimbach 2013). A distinct ad-
102 vantage of performing a heat budget analysis in a high-resolution, data-assimilating state estimate

¹⁰³ such as the Southern Ocean State Estimate (SOSE) is that the mass and heat budgets are closed at
¹⁰⁴ every grid point and vertical advective and diffusive processes are explicitly resolved or parame-
¹⁰⁵ terized in the model. Additionally, numerous ocean observations in state estimates constrain the
¹⁰⁶ large scale upper ocean state so that the model representation of upper ocean stratification is con-
¹⁰⁷ sistent with observations, making it possible to explore the three-dimensional heat budget within
¹⁰⁸ the upper ocean.

¹⁰⁹ The goal of this study is to examine the ocean dynamics governing regions of ocean heat gain and
¹¹⁰ loss along the ACC by analyzing the heat budget in the eddy-permitting, data-assimilating SOSE.
¹¹¹ This Southern Ocean heat budget analysis is timely and novel because of the great improvement in
¹¹² air-sea fluxes through ocean state estimation compared with atmospheric reanalyses (Cerovecki et
¹¹³ al., 2011) and the ability to fully close the heat budget at every grid point using the state estimate's
¹¹⁴ fields. Additionally, this will provide insight into the role of surface heat flux as a component
¹¹⁵ of buoyancy forcing in setting the three dimensional structure and strength of the upper cell of
¹¹⁶ the Southern Ocean meridional overturning circulation. In section 2 we describe the model and
¹¹⁷ methods used in calculating the heat budget. The adjusted air-sea heat fluxes in the model are
¹¹⁸ discussed in section 3, the heat budget and spatial and seasonal variability are analyzed in section
¹¹⁹ 4. The results and conclusions are summarized in section 5.

¹²⁰ 2. Model and methods

¹²¹ a. *The Southern Ocean State Estimate*

¹²² The SOSE (Mazloff et al. 2010) is an eddy permitting, data assimilating model developed using
¹²³ software developed by the consortium for Estimating the Climate and Circulation of the Ocean
¹²⁴ (ECCO; <http://www.ecco-group.org>). The SOSE ocean dynamics is represented using the MIT-

125 gcm (Marshall et al. 1997). The present configuration of the model has 1/6°horizontal resolution
126 and 42 vertical levels in the domain from 24.7°S to 78°S with an open northern boundary and a
127 900-s time step and sub-grid parameterizations as described in Mazloff et al. (2010). Using an
128 adjoint method, the model is fit to the majority of available observations in the Southern Ocean
129 to minimize the squared difference between the model and observations iteratively by adjusting
130 the “control vector” which consists of the initial conditions and atmospheric state. The initial and
131 northern open boundary conditions are from a 1°global state estimate (Forget 2010) and the initial
132 atmospheric state is constrained by the ECMWF ERA-interim global reanalysis (Dee et al. 2011).
133 Momentum, heat and freshwater fluxes between the atmosphere and ocean are determined using
134 bulk formulae (Large and Yeager 2009). The thermodynamic sea ice model is similar to that de-
135 scribed by Fenty and Heimbach (2013) and includes albedo as a function of surface ice conditions
136 and turbulent air-ice fluxes calculated using standard bulk aerodynamic formulae. The SOSE so-
137 lution has been extensively validated and compared to observations (e.g. Cerovečki et al. 2013).
138 The SOSE adjusted air-sea fluxes have been validated against other available flux products and are
139 consistent with the best modern flux estimates (Cerovečki et al. 2011). As expected, the largest
140 differences between SOSE and other flux products tend to be in regions with strong mesoscale
141 activity such as the ACC and western boundary currents.

142 *b. Heat budget analysis*

143 The SOSE iteration 100 solution used for this analysis is a 6-year (2005-2010), updated version
144 of the solution described by Mazloff et al. (2010). Terms in the heat and salt budgets are diagnosed
145 at each grid point from the model state and output as 5-day averages. The time evolution of
146 temperature in the ocean is given by the sum of net heat exchange with the atmosphere, divergence

¹⁴⁷ of advective heat transport by both geostrophic horizontal, ageostrophic horizontal and vertical
¹⁴⁸ velocities, and 3-dimensional diffusive processes:

$$\underbrace{\frac{\partial T}{\partial t}}_{\text{temperature tendency}} = \underbrace{\frac{Q(z)}{\rho c_p dz}}_{\text{air-sea flux}} - \underbrace{\mathbf{u}_g \cdot \nabla_H T}_{\text{geostrophic advection}} - \underbrace{\mathbf{u}_a \cdot \nabla_H T}_{\text{ageostrophic advection}} - \underbrace{w \cdot \frac{\partial T}{\partial z}}_{\text{vertical advection}} + \underbrace{\kappa_H \nabla_H^2 T + \kappa_z \frac{\partial^2 T}{\partial z^2} + K_T^{turb}}_{\text{diffusion}} \quad (1)$$

¹⁴⁹ where T is potential temperature, $\partial T / \partial t$ is the temperature tendency, Q is the net air-sea heat
¹⁵⁰ flux in W/m^2 (positive is heat flux into the ocean) which includes depth-dependent shortwave
¹⁵¹ radiation distributed vertically over several upper model layers, ρ is the density, c_p is the specific
¹⁵² heat capacity of seawater, dz is the thickness of the model layer over which Q is distributed, \mathbf{u}_g
¹⁵³ and \mathbf{u}_a are the geostrophic and ageostrophic horizontal velocity vectors, respectively, ∇_H is the
¹⁵⁴ horizontal divergence operator, w is the vertical velocity, κ_H and κ_z are the horizontal and vertical
¹⁵⁵ diffusivity respectively, and K_T^{turb} is the K-profile parameterization turbulent vertical diffusion term
¹⁵⁶ (Large et al. 1994). In SOSE, penetration of downward shortwave radiation below the surface is
¹⁵⁷ based on an assumption of exponential decay with depth (Paulson and Simpson 1977), following
¹⁵⁸ Jerlov (1968)

$$Q(z) = Q(0) \left[R \exp \left(\frac{z}{\gamma_1} \right) + (1 - R) \exp \left(\frac{z}{\gamma_2} \right) \right] \quad (2)$$

¹⁵⁹ where $Q(0)$ is the downward shortwave radiation at the sea surface, z is depth and R , γ_1 and γ_2
¹⁶⁰ are constants for water type IB as defined by Jerlov (1968). Shortwave radiation typically decays
¹⁶¹ to 10% of its surface value in the upper 25 m and to below 1% by 75 m, so the heat budget solution
¹⁶² is only significantly affected by the choice of water type in the upper 50 m. Geostrophic velocities
¹⁶³ were calculated for this analysis from the model hydrostatic pressure, and ageostrophic veloci-
¹⁶⁴ ties were calculated here as the residual between the model velocity and calculated geostrophic

₁₆₅ velocity. Geostrophic horizontal advection and vertical advection were further decomposed into
₁₆₆ time-mean and transient eddy advection terms

$$\overline{u'_g T'} = \overline{u_g T} - \overline{u_g} \overline{T} \quad (3)$$

$$\overline{w' T'} = \overline{w T} - \overline{w} \overline{T} \quad (4)$$

₁₆₇ where overbars denotes a 3-month seasonal mean and primes denote a deviation from this mean
₁₆₈ for each season in the 6-year model run. This eddy definition is chosen based on the decorrelation
₁₆₉ time scale of 34 days in the ACC estimated from altimeter data by Gille and Kelly (1996).

₁₇₀ For brevity, each of the terms in equation 1 will be referred to using the label indicated on the
₁₇₁ equations. For example, divergence of geostrophic temperature transport will be referred to simply
₁₇₂ as the geostrophic advection term. In the analysis the heat budget solution will be examined in
₁₇₃ two ways. First, horizontal maps of the heat budget terms in equation 1 at each grid point are
₁₇₄ presented to show major spatial patterns in the heat budget terms. Second, to focus more closely
₁₇₅ on zonal variations in the heat balance the grid point solution is integrated meridionally between
₁₇₆ ACC streamlines and vertically over the upper ocean. Identifying a robust streamline in the ACC
₁₇₇ is difficult due to the non-stationary and segmented fronts of the ACC but we choose to define
₁₇₈ streamlines using sea surface height contours following numerous previous studies (e.g. Sokolov
₁₇₉ and Rintoul 2009). The upper boundary of integration is the ocean surface and the lower boundary
₁₈₀ is chosen as the grid point at 624 m which is below the deepest winter mixed layers where the
₁₈₁ spatially averaged temperature variance is greatly reduced, encompassing the top 20 model layers.
₁₈₂ The heat budget terms are integrated to a constant depth level rather than an isopycnal surface,
₁₈₃ as this simplifies the analysis and volume is conserved. Modest adjustments to the depth of the
₁₈₄ lower boundary have little influence on the conclusions presented except that a shallower boundary

¹⁸⁵ results in significant increase in size of the vertical diffusion term in the Southeast Indian and
¹⁸⁶ Southeast Pacific basins where deep winter mixed layers can extend below 624 m (Dong et al.
¹⁸⁷ 2007).

¹⁸⁸ **3. Heat Budget**

¹⁸⁹ *a. Time-mean air-sea heat flux*

¹⁹⁰ The most prominent feature of the net time-mean air-sea heat flux in the SOSE solution is the
¹⁹¹ intense cooling associated with the western boundary current regions, particularly the Agulhas
¹⁹² Return Current (ARC) flowing eastward across the Indian Ocean east of South Africa (Fig. 1b).
¹⁹³ South of these heat loss regions in the Atlantic and Indian basins, between Drake Passage (DP) at
¹⁹⁴ 60°W and Campbell Plateau (CP) at 170°E, is a broad region of ocean heat gain at ACC latitudes
¹⁹⁵ which is strongest in the northern extension of the ACC at the Malvinas Current and south of the
¹⁹⁶ ARC in the Indian sector. The Pacific Ocean sector, from CP east to DP, is dominated by relatively
¹⁹⁷ small magnitude net surface ocean heat loss, in contrast to the rest of the ACC, but in a given year
¹⁹⁸ the annual-mean heat flux can be weakly positive or negative. The broad scale coherent patterns
¹⁹⁹ of heat gain and weak loss in SOSE are consistent with other recent air-sea heat flux products
²⁰⁰ (Large and Yeager 2009; Cerovečki et al. 2011) despite mesoscale variations in SOSE fluxes due
²⁰¹ to adjustments to the oceanic observations, indicating that these large-scale features are robust.
²⁰² For the remainder of this paper, Atlantic/Indian refers to the Southern Ocean sector bounded on
²⁰³ the west by DP and east by CP, and Pacific refers to the remaining section of the Southern Ocean.
²⁰⁴ We argue that this definition of two sectors of the ACC based on topographic features is more
²⁰⁵ appropriate to the dynamics and air-sea exchanges in the circumpolar Southern Ocean than the
²⁰⁶ three major basin definitions typically used.

207 The spatial pattern in the SOSE net air-sea heat flux zonal anomaly (Fig. 1c) is dominated by
208 latent heat flux (Fig. 1f) and less so by the sensible heat flux (Fig. 1g). Shortwave (Fig. 1d) and
209 longwave (Fig. 1e) components show relatively small spatial variation, apart from a meridional
210 gradient, and tend to compensate one another. Sensible heat flux depends directly on the air-sea
211 temperature difference, ΔT , while latent heat flux depends indirectly on ΔT through the influence
212 of temperature on the air-sea humidity difference, Δq . Wind speed also modulates the strength of
213 these turbulent fluxes but is not the dominant control as wind speed can act to amplify the flux
214 but requires the presence of a temperature or humidity gradient. Therefore, latent and sensible
215 heat fluxes tend to respond to spatial patterns and variability in sea surface temperature (SST)
216 (Yu and Weller 2007) and to spatial patterns in atmospheric temperature. The SOSE time mean
217 zonal anomaly of SST (Fig. 1a) is dominated by a dipole with colder SST in the Atlantic/Indian
218 and warmer SST in the Pacific, which is consistent with the pattern in air-sea flux. Atmospheric
219 temperature also shows a zonally asymmetric pattern similar to SST and net air-sea heat flux,
220 with the quasi-stationary zonal wave 1, defined as the first zonal harmonic of the geopotential
221 height field, accounting for up to 90% of the Southern Hemisphere mean spatial distribution in
222 atmospheric pressure (van Loon and Jenne 1972; Hobbs and Raphael 2010). Milliff et al. (1999)
223 suggested the zonal wave 1 pattern may represent a coupled ocean-atmosphere mode and Hobbs
224 and Raphael (2007) find statistically significant correlations between SST and atmospheric zonal
225 wave 1 throughout much of the Southern Ocean.

226 *b. Time-mean heat budget*

227 In all regions in the Southern Ocean the dominant balance in the upper ocean, integrated over the
228 upper 624 m, is between air-sea flux (Fig. 2a) and the total divergence of temperature advection
229 (Fig. 2b) while diffusion is negligible. Separated geostrophic, ageostrophic and vertical advection

230 terms locally display positive and negative values an order of magnitude larger than the air-sea flux
231 values, which cancel in the advective sum, particularly in ACC latitudes and western boundary
232 current regions which have high eddy kinetic energy. The geostrophic advection term (Fig. 2c)
233 tends to be positive (increasing temperature tendency) in the western boundary current and ACC
234 latitudes and is negative in the subtropical gyre regions where there is equatorward flow and a
235 strong meridional temperature gradient.

236 The ageostrophic advection term (Fig. 2d) is negative through most of the domain, decreasing
237 the temperature, due to Ekman transport driven by westerly winds bringing cold water equator-
238 ward. Ekman transport calculated from SOSE wind stress accounts for > 90% of the variance in
239 ageostrophic transport in most locations and differences are localized close to shallow topography
240 and in regions with high eddy variability (Fig. A1). In these locations, we expect ageostrophic
241 processes other than Ekman transport to be important at scales smaller than the Rossby radius of
242 deformation (Rocha et al. 2015) which are at the limit of the smallest scales that are resolved in
243 SOSE (Chelton and Deszoeke 1998). However, when integrated the contribution of these non-
244 Ekman ageostrophic transports to the total ageostrophic transport is negligible (Mazloff et al.
245 2010) (see appendix for more details).

246 The vertical advection term (Fig. 2e) is generally positive (heating the upper ocean) in sub-
247 tropical regions due to downwelling driven by Ekman pumping associated with wind stress curl.
248 It is also positive along the Antarctic continental shelf where the vertical temperature gradient is
249 reversed with colder water at the surface and relatively warm water upwelling from below. Within
250 the ACC, but outside of locations with high eddy activity, the vertical advection term is negative
251 (cooling) as upwelling brings colder waters toward the surface.

252 The diffusion term (Fig. 2f) is negligible when integrated vertically over the upper 624 m apart
253 from deep water formation regions along the Antarctic coast which will not be considered in this

analysis. Although diffusion is small in the depth-integrated budget, diffusion is an important term in the mixed layer and is responsible for a large vertical redistribution of heat within the mixed layer. This contribution to the heat budget is confined to within the upper 100 - 200 m in most locations and positive and negative signals cancel when vertically integrated to depths below the mixed layer.

The temperature tendency (Fig. 2g) is small due to the cancellation between the air-sea heat flux and total divergence of temperature transport (Fig. 2a,b), but shows some large scale spatial patterns. Given that the model run spans only 6 years, the patterns in the temperature tendency are most likely due to interannual variability rather than a long term trend. Comparison with the temperature tendency in Argo gridded data over the same time period shows similar spatial structure but SOSE displays slightly larger magnitudes which may be due to small model drift. However, the magnitude of the trends are small relative to the total temperature variability.

The mean, $\bar{\mathbf{u}}_g \cdot \nabla_H \bar{T}$ (Fig. 3a), and eddy, $\mathbf{u}'_g \cdot \nabla_H T'$ (Fig. 3b), components of the geostrophic advection term are of similar magnitudes (Fig. 3a). However, the eddy term is small except in regions with high eddy variability in western boundary currents and in the ACC. In particular, divergence of eddy heat flux is large downstream of topographic features including Kerguelen Plateau (60-80°E), Macquarie Ridge (150°E) and the Pacific-Antarctic Ridge (150°W) as well as CP and DP (Fig. 3b), consistent with observed enhancement of eddy kinetic energy and cross-frontal transport in these regions (Chelton et al. 1990; Thompson and Sallee 2012).

The mean component of the vertical advection term, $\bar{w} \frac{\partial \bar{T}}{\partial z}$ (Fig. 3c), like the geostrophic advection term, dominates the total vertical advection term outside of the energetic western boundary currents and ACC. The mean vertical advection term is strongly negative downstream of Kerguelen Plateau, at the Pacific-Antarctic Ridge and east of DP corresponding to locations where the eddy component of the vertical advection term, $w' \frac{\partial T'}{\partial z}$ (Fig. 3d), is positive, hence with strong

compensation between the time-mean and eddy components in these locations (Fig. 3c,d). The spatial pattern in the vertical eddy advection term is similar to that of the eddy component of the geostrophic advection term and is positive in most regions, suggesting that this represents the vertical component of along-isopycnal eddy heat flux, which leads to warming by upward eddy flux along poleward tilted isopycnals with an along-isopycnal temperature gradient (Wolfe et al. 2008).

Figure 4b shows the vertically integrated terms that are mapped in Figure 2, also integrated meridionally within the ACC. ACC boundaries are defined as the outermost time-mean sea surface height (SSH) lines that are closed through DP (Fig. 4a). There are apparent large magnitude, short wavelength variations in the advection terms that are concentrated in ‘hotspots’ close to coastlines and shallow topography and in eddy-rich regions which dominate the larger scale signals (Fig. 4b).

To more clearly visualize how each heat budget term varies as a function of longitude, the vertically and meridionally integrated terms (Fig. 4b) are cumulatively summed with longitude (Fig. 4c). There is net ocean heat gain in the circumpolar integral although the pattern of air sea heat gain in the Atlantic/Indian sector and air-sea heat loss in the Pacific is apparent. As in Figure 2, the total geostrophic advection term is generally negative or negligible in the Atlantic/Indian sector and positive throughout the Pacific sector of the ACC, with the exception of a region from 70-100°E in the Indian sector, downstream of Kerguelen Plateau and 0-30°W, at the Brazil-Malvinas Confluence where it is also positive. This localized region of convergence of geostrophic heat advection downstream of Kerguelen Plateau is likely due to warm, subtropical ARC waters crossing the Subantarctic Front southward into the ACC downstream of Kerguelen Plateau (Wang et al. 2014). Similarly, downstream of Drake Passage the positive geostrophic advection term can be attributed to cross-frontal flow of subtropical Brazil Current waters into the ACC. Again, the ageostrophic advection term is consistently negative at all longitudes along the ACC associated with northward

302 Ekman transport of colder water (Fig. A1). The total vertical advection term has a weak net
303 cooling effect, with localized contributions at major topographic features implying topographic
304 control of vertical heat exchange (Fig. 4c). The cumulative sum of temperature tendency shows
305 that small positive and negative temperature trends, when summed cumulatively along the ACC,
306 are a reassuringly small contribution to the heat budget. The cumulatively summed diffusion term
307 is negligible (Fig. 4c).

308 Decomposition of the horizontal geostrophic and vertical advection components into contribu-
309 tions from the mean flow and transient eddies (Fig. 4d) shows that both horizontal and vertical
310 eddy heat flux divergence are warming the upper ocean. This warming by eddy heat flux diver-
311 gence is confined to localized regions, predominantly downstream of the Kerguelen Plateau where
312 warm ARC waters reach the ACC and, to a lesser extent, the Macquarie Ridge. In the circumpolar
313 integral, the mean and eddy components of the geostrophic advection term are of similar magni-
314 tude. However, the mean geostrophic advection term (Fig. 4d) is responsible for the majority of
315 the zonal variation observed in the total geostrophic advection term (Fig. 4c). There is substan-
316 tial cancellation between the mean and eddy components of the vertical advection term leading to
317 weak net cooling by the total vertical advection term which is consistent with previous modeling
318 studies of vertical heat flux (Wolfe et al. 2008; Morrison et al. 2013). Both the mean and eddy
319 components of the vertical heat advection term are concentrated downstream of major topographic
320 features, and are generally negligible elsewhere. Due to the cancellation between mean and eddy
321 vertical heat fluxes, the net contribution to the heat budget is small relative to the horizontal ad-
322 vection terms, and likely has been overestimated in studies which do not include eddy heat fluxes
323 (Dong et al. 2007). Note that because the heat budget is integrated to a constant depth level rather
324 than an isopycnal, there are vertical displacements in isopycnals along the ACC path which may
325 appear as vertical heat flux which are not associated with diapycnal vertical velocities.

326 The mean temperature along the ACC path (Fig. 4c, dashed black), averaged vertically and
327 between the two sea surface height contours in Fig. 4a, shows that the ACC is warmer in the
328 Atlantic/Indian sector and cooler in the Pacific sector. The ACC mean temperature ranges from
329 3°C in the southeast Pacific to 6°C in the Atlantic, which is a significant temperature difference as
330 SOSE temperature variance is of the order 1°C in the core of the ACC. Sun and Watts (2002) also
331 found that the ACC is warmer along streamlines in the Atlantic and Indian sectors and cooler in the
332 Pacific and attributed the dominant source of heat for the ACC to the Brazil Current and Agulhas
333 Return Current (ARC). Our results support this result, but indicate that horizontal advection in the
334 Atlantic/Indian sector is not solely responsible for the heat content variation along the ACC, that
335 is, air-sea heat fluxes contribute about half of the necessary heat input (Fig. 4c). The temperature
336 difference along the mean path of the ACC also has important implications for the contribution of
337 the mean flow to poleward heat transport in the Southern Ocean as the poleward flowing section of
338 the ACC carries more heat than the equatorward flowing Malvinas Current (Sun and Watts 2002).

339 The circumpolar integral of terms shown in Fig 4, as well as integrated over the Atlantic/Indian
340 and Pacific sectors separately are listed in Table 1. The total, integrated air-sea flux in the ACC is
341 0.27 PW ocean heat gain, with heat gain of 0.35 PW in the Atlantic/Indian sector in contrast with -
342 0.08 PW heat loss in the Pacific sector. As is the case for air-sea heat flux, the sign of the time-mean
343 geostrophic advection term differs between the two regions, with -0.01 PW in the Atlantic/Indian
344 and 0.24 PW in the Pacific. The contributions to the circumpolar integrated horizontal and vertical
345 eddy advection terms are dominated by the Atlantic/Indian sector because this sector captures all
346 of the major eddy-producing topographic features along the ACC path excluding CP and Pacific-
347 Antarctic Ridge. The circumpolar integral of the geostrophic advection term is 0.38 PW and
348 along with 0.27 PW air-sea heat gain is balanced by -0.58 PW cooling due to the ageostrophic
349 advection term and -0.09 PW cooling due to the total vertical advection term. Thus, in the cir-

350 cumpolar integral, the dominant balance is between the positive total geostrophic advection and
351 air-sea flux terms and the negative ageostrophic advection term. However, when integrated over
352 each ocean basin separately, in the Atlantic/Indian sector air-sea heat gain and the eddy component
353 of geostrophic advection balance cooling by the ageostrophic advection term, while in the Pacific
354 sector the mean geostrophic advection term balances cooling by the ageostrophic advection term
355 and air-sea heat loss. The time-mean temperature tendency is small but negative (cooling) over the
356 entire ACC although this signal is confined to the Pacific sector where air-sea flux is negative.

357 *c. Seasonal variability*

358 The time-mean heat budget is the residual of a much larger seasonal cycle, where seasonal vari-
359 ation in temperature tendency is dominated by the seasonal cycle in air-sea heat flux (Fig. 5). The
360 circumpolar integrated ACC air-sea heat flux ranges from -2 PW in winter to 3 PW in summer and
361 is closely mirrored by the temperature tendency, with a small negative offset due to net cooling by
362 the sum of the geostrophic, ageostrophic and vertical advection terms. Notably, the ageostrophic
363 advection term does not show a strong seasonal cycle, differing from a previous observational
364 study (Dong et al. 2007). This may be attributed to seasonal variations in the mixed layer depth
365 boundary of the mixed layer model of Dong et al. (2007), whereas a constant depth of integra-
366 tion is used in this analysis or variability in the small non-Ekman component of the ageostrophic
367 advection term on non-seasonal timescales. However, the magnitude of the ageostrophic advec-
368 tion term is slightly larger in winter and spring (Fig. 5c,e), consistent with the seasonal cycle in
369 the strength and position of westerly winds that force the Ekman transport. The magnitude and
370 zonal patterns in the geostrophic and vertical advection terms and their corresponding mean and
371 eddy components do not show significant seasonal variation, consistent with the conclusion that

372 the spatial variations in the advection terms are related to topographic features and intrinsic ocean
373 variability.

374 Time series of the 3-month averaged, depth-integrated heat budget integrated in the At-
375 lantic/Indian and Pacific sectors separately (similar to Table 1) demonstrate the large seasonal
376 cycle in temperature tendency that closely follows air-sea heat flux in magnitude and sign but with
377 a slight negative offset as a result of the sum of the seasonal mean advection terms in the budget
378 (Fig. 6 a and b). Temporal variations in the seasonally-averaged advection terms are relatively
379 small and unlike air-sea heat flux, the sign of the advective terms remains constant in all seasons.
380 Note that there is substantial variability in the heat budget terms on shorter timescales which is
381 not considered in this analysis. There is a significant difference in the geostrophic advection term
382 between the Atlantic/Indian and Pacific sectors which is of a similar magnitude to the difference in
383 air-sea heat flux (Fig. 6c), but the difference in vertical and ageostrophic advection terms between
384 the two regions is small relative to the standard deviation of these terms. This result indicates that
385 the mean geostrophic advection term differs spatially due to the meridional shift in the position
386 of the ACC along its path, with small divergence of geostrophic temperature advection in the At-
387 lantic/Indian where the ACC is equatorward of its mean position and convergence of geostrophic
388 temperature advection in the Pacific sector where the ACC is further poleward. This zonal differ-
389 ence in geostrophic heat transport is mostly balanced by the zonal difference in air-sea heat flux,
390 leading to only a small temperature tendency difference between the two regions.

391 *d. Comparison with the Agulhas Return Current*

392 Poleward flowing western boundary currents are sites of intense ocean heat loss as warm, sub-
393 tropical water flows toward the poles under a colder atmosphere (Vivier et al. 2002; Dong and
394 Kelly 2004; Roemmich et al. 2005). This difference is particularly striking in the Agulhas Current

395 and ARC region where there is a sharp meridional transition between the heat loss in the ARC
396 north of the Subantarctic front, and the heat gain in the ACC south of the front (Fig. 7a). The
397 ocean heat loss in the poleward flowing Pacific sector of the ACC is similar to that in extensions
398 of poleward flowing western boundary currents, particularly the ARC. Therefore, it is useful to
399 compare and contrast the heat budget in these two regions. Dong et al. (2007) found the largest
400 imbalances in their heat budget inferred from observations in the Brazil/Falkland and ARC re-
401 gions suggesting that unresolved small-scale advective processes and strong air-sea coupling are
402 important to the heat budget in these regions (e.g. O'Neill et al. 2003, 2005). Fig 7 shows the
403 time-mean integrated heat budget solution in the ARC region similar to that shown in Figure 4
404 for the ACC. The geostrophic advection and vertical advection terms are positive, warming the
405 ARC downstream of the Agulhas retroflection although the magnitude of this warming varies sig-
406 nificantly due to standing meanders along the ARC (Fig. 7b). This is balanced by cooling from
407 air-sea heat loss and the Ekman advection term (weaker than in the ACC), consistent with previ-
408 ous analyses in western boundary currents which indicate that geostrophic advection is the major
409 warming term (Dong and Kelly 2004; Roemmich et al. 2005).

410 Decomposition of the mean and eddy components of horizontal and vertical advection (Fig. 7c)
411 shows that the horizontal geostrophic advection term is strongly positive, bringing warm subtropi-
412 cal water into the region. The eddy component of the geostrophic advection term is negative lead-
413 ing to substantial cancellation between the mean and eddy contributions to the total geostrophic
414 advection term. Both the mean and eddy vertical advection terms are positive in the ARC. The
415 sign of the mean vertical heat advection is reversed compared to the ACC because wind stress
416 curl drives downwelling of warmer surface water rather than upwelling at this latitude. Interest-
417 ingly, the ARC heat balance is somewhat similar to the dominant balance in the Pacific sector
418 of the ACC (Fig. 4c), where total geostrophic advection warms the upper ocean and is balanced

419 by cooling from both air-sea fluxes and Ekman advection. At first glance, we expect the Pacific
420 sector of the ACC and the ARC to differ due to the larger spatial scale and stronger Ekman
421 transport in the ACC. However, the Pacific sector of the ACC is analogous to the poleward flow
422 of a western boundary current: when the ACC reaches the Pacific it has warmed and meanders
423 southward at CP bringing relatively warm waters under a cooler atmosphere. There are notable
424 differences between the ARC and the Pacific sector of the ACC: air-sea heat loss is the dominant
425 cooling term in the ARC, whereas in the Pacific sector of the ACC cooling from air-sea fluxes is
426 weaker and cooling by the Ekman advection term dominates. Also, both mean and eddy vertical
427 advection terms contribute to net warming in the ARC while in the Pacific sector of the ACC the
428 vertical advection term is cooling with substantial cancellation between the time-mean and eddy
429 components (Fig. 4d).

430 Time series of the ARC (not shown) indicate that both air-sea fluxes and geostrophic and Ek-
431 man advection terms contribute to seasonal variations in temperature tendency, unlike in the ACC
432 where the tendency is dominated by air-sea fluxes only (Fig. 6d). The variance in the geostrophic
433 advection term in the ARC is dominated by large non-seasonal variations in the transport and re-
434 calculations in the current, obscuring the seasonal cycle. The resulting temperature tendency over
435 the entire ARC has a smaller seasonal cycle than the ACC although on small scales the tendency
436 variability can be much larger. In this highly energetic region, the quantitative heat budget results
437 are sensitive to the boundaries of integration but the sign of the integrated terms does not change
438 and the qualitative result remains consistent. While the role of geostrophic advection in the time-
439 averaged heat budget is similar in the ARC and the Pacific sector of the ACC, the variability in
440 the geostrophic advection term in the ARC is much larger than in the ACC, unsurprising given the
441 large variability in transport due to recalculations in the ARC.

⁴⁴² **4. Summary and Conclusions**

⁴⁴³ We have analyzed the 3-dimensional spatial variations and seasonal variability in the upper
⁴⁴⁴ ocean heat budget of the ACC in SOSE for the years 2005-2010. SOSE is eddy permitting, well-
⁴⁴⁵ constrained by ocean observations in the upper ocean and has closed budgets, allowing novel
⁴⁴⁶ analysis of the heat budget in the Southern Ocean where previous studies of the heat budget have
⁴⁴⁷ been limited by sparse observations, unresolved mesoscale processes and inadequate surface heat
⁴⁴⁸ fluxes, leading to large imbalances in the heat budget (Dong et al. 2007).

⁴⁴⁹ • Large scale patterns of air-sea heat fluxes from SOSE agree with the best independent heat
⁴⁵⁰ flux products, i.e. Large and Yeager (2009) (Cerovečki et al. 2011), showing a robust zonally
⁴⁵¹ asymmetric pattern in the ACC, with ocean heat gain in the Atlantic/Indian sector and ocean
⁴⁵² heat loss in the Pacific sector.

⁴⁵³ • In the Atlantic/Indian sector of the ACC, ocean heat gain is opposed by cooling by divergence
⁴⁵⁴ of ageostrophic temperature advection due to Ekman transport, consistent with Dong et al.
⁴⁵⁵ (2007) and Sallée et al. (2006). Warming due to divergence of geostrophic eddy heat flux and
⁴⁵⁶ cooling due to divergence of vertical temperature advection play a lesser role.

⁴⁵⁷ • In the Pacific sector of the ACC, both ocean heat loss to the atmosphere and cooling by
⁴⁵⁸ the divergence of ageostrophic temperature advection due to Ekman transport is balanced
⁴⁵⁹ by a convergence of geostrophic heat advection. The warming by divergence of geostrophic
⁴⁶⁰ temperature advection is achieved almost entirely by the mean geostrophic flow, unlike in the
⁴⁶¹ Atlantic/Indian sector the mean component is insignificant and instead is dominated by eddy
⁴⁶² heat flux divergence downstream of topographic features.

- Comparison of the ACC heat budget with the poleward-flowing, subtropical ARC suggests the dominant heat balance in the Pacific sector of the ACC is similar to that in the ARC despite different spatial scales.
- Divergence of both horizontal and vertical transient eddy heat flux causes significant warming in narrow regions downstream of major topographic features where there is enhanced mesoscale energy (e.g. Naveira Garabato et al. 2011).
- There is a large seasonal cycle in air-sea heat flux which dominates the seasonal cycle of temperature tendency.

We have demonstrated that mean geostrophic temperature advection is a dominant component of the Southern Ocean heat budget due to meridional standing meanders of the ACC and inflow of warm, subtropical boundary current waters into the ACC across the subantarctic front. This supports the inference of Sun and Watts (2002) that since heat content varies along the mean ACC path there must be an associated net poleward heat transport. Sun and Watts (2002) concluded that subtropical water, particularly from the Brazil-Malvinas Confluence, is responsible for the variation in heat content along the ACC mean path. However, our results indicate that air-sea heat flux is also a major source of heat to the ACC mean flow in the Atlantic/Indian sector; this difference is likely due to availability of modern flux products that were not available to Sun and Watts (2002). The ACC gains heat from the atmosphere when it flows northward in the Malvinas Current and throughout the Indian and Atlantic sectors, in addition to heat input by the Brazil Current and ARC, and releases some of this heat back to the atmosphere as it flows southward in the Pacific. This phenomenon is analogous to the heat exchange by horizontal gyre circulations, and we show that the ACC budget in the Pacific is similar to the budget that arises as relatively warm waters are advected poleward in the ARC.

486 The dominant role of northward Ekman transport is indicative of the surface branch of the up-
487 per cell of the Southern Ocean overturning circulation, with ocean heat gain throughout the At-
488 lantic/Indian sector transforming Antarctic Surface Water to lighter water as it is advected equa-
489 torward. In the Pacific where the net heat flux is not strongly positive, freshwater fluxes dominate
490 surface buoyancy gain and advection of heat by the mean geostrophic flow adds buoyancy neces-
491 sary for the upper cell of the overturning circulation. Further work is needed to quantify the salt
492 budget in SOSE, however freshwater flux in SOSE lacks the strongly zonally asymmetric signal
493 seen in heat flux, and so the zonal pattern in buoyancy forcing is dominated by air-sea heat flux
494 (Cerovečki et al. 2013). In an idealized model using a sinusoidal zonal pattern of buoyancy forc-
495 ing, Radko and Marshall (2006) found that the larger buoyancy gain in the Atlantic/Indian sector
496 of the Southern Ocean leads to stronger overturning. However, further work is needed to investi-
497 gate the zonal variation in overturning strength using a more realistic spatial pattern of buoyancy
498 forcing, and in a more realistic model or using observations.

499 Our results have important implications for climate models; it implies that models must have
500 accurate spatial correlations between mean velocity and temperature fields in order to simulate the
501 poleward heat flux by the ACC. Low resolution models which approximate the total ACC vol-
502 ume transport well but lack the narrow, intense jets and meandering structure of the current may
503 be misrepresenting heat transport by the mean ACC flow (e.g. Dufour et al. 2012). Additionally,
504 models that do not resolve eddies accurately lack the important contribution of warming by di-
505 vergence of eddy heat flux to the heat budget in regions downstream of topography. While SOSE
506 at 1/6°resolves the ACC jet structure better than global coarse-resolution models, there are unre-
507 solved finer scale processes that may alter the mean geostrophic heat flux. Further work is needed
508 with the next generation of higher resolution products to explore the impact of model resolution
509 on mean ACC heat transport.

510 Because of the importance of air-sea heat and freshwater fluxes in determining the strength of
511 the upper cell of the overturning circulation (Radko and Marshall 2006), the pronounced zonal
512 asymmetry in the ACC heat budget shown in this work illustrates the need for further work to
513 understand the three-dimensional structure of the overturning circulation in the Southern Ocean.
514 Understanding how observed and predicted future changes in buoyancy and wind forcing will alter
515 the strength of the overturning circulation is a necessary step toward understanding the role of the
516 Southern Ocean in future uptake and storage of heat, carbon and nutrients.

517 *Acknowledgments.* This work was supported by NSF grant OCE1357072. Computational
518 resources for the Southern Ocean State Estimate were provided by NSF XSEDE resource
519 grant OCE130007. The SOSE iteration 100 solution is freely available for download
520 (<http://sose.ucsd.edu>). We thank an anonymous reviewer for comments which improved the quality
521 of this manuscript.

522 APPENDIX

523 Comparison between Ekman transport from winds and ageostrophic transport.

524 Here we briefly show a comparison between Ekman transport calculated from wind stress and
525 ageostrophic transport calculated from the residual between total and geostrophic velocities in
526 the Southern Ocean State Estimate. The components of Ekman transport, U_{ek} and V_{ek} ($\text{m}^2 \text{ s}^{-1}$)
527 integrated over the Ekman depth, d_{ek} , are estimated from the SOSE zonal and meridional mean
528 wind stress fields, $\bar{\tau}^x$ and $\bar{\tau}^y$, according to the relations $U_{ek} = \frac{\bar{\tau}^y}{\rho f}$ and $V_{ek} = \frac{\bar{\tau}^x}{\rho f}$, where ρ is the
529 density and f is the Coriolis parameter. The ageostrophic transport, U_{ag} , is estimated by taking
530 the difference between the total velocity, u , and the geostrophic velocity calculated from the SOSE
531 pressure field, u_g , and integrating vertically from the surface to d_{ek} such that $U_{ag} = \int_{-d_{ek}}^0 (u - u_g) dz$.

532 For this comparison we assume a constant Ekman depth of 100 m, based on observations of Ekman
533 transport in the Drake Passage (Lenn and Chereskin 2009); however the qualitative difference
534 between the Ekman and ageostrophic transports is not sensitive to this choice.

535 Figure A1 shows that the differences between the zonal and meridional components of Ekman
536 transport and ageostrophic transport are concentrated in energetic regions particularly western
537 boundary currents and close to major topographic features where ageostrophic transport dues to
538 processes other than Ekman transport are expected. These differences are noisy and don't have a
539 sign preference. Thus when the ageostrophic advection is integrated meridionally and zonally, the
540 non-Ekman contributions are not significant and the ageostrophic transport is a good approxima-
541 tion to the Ekman transport.

542 References

- 543 Bourassa, M. A., and Coauthors, 2013: High-Latitude Ocean and Sea Ice Surface Fluxes: Chal-
544 lenges for Climate Research. *Bulletin of the American Meteorological Society*, **94** (3), 403–
545 423, doi:10.1175/BAMS-D-11-00244.1, URL <http://journals.ametsoc.org/doi/abs/10.1175/BAMS-D-11-00244.1>.
- 547 Cerovečki, I., M. R. Mazloff, and L. D. Talley, 2011: A Comparison of Southern Ocean Air-
548 Sea Buoyancy Flux from an Ocean State Estimate with Five Other Products. *Journal of Cli-
549 mate*, **24** (24), 6283–6306, doi:10.1175/2011JCLI3858.1, URL <http://journals.ametsoc.org/doi/abs/10.1175/2011JCLI3858.1>.
- 551 Cerovečki, I., L. D. Talley, M. R. Mazloff, and G. Maze, 2013: Subantarctic Mode Water
552 Formation, Destruction, and Export in the Eddy-Permitting Southern Ocean State Estimate.

553 *Journal of Physical Oceanography*, **43** (7), 1485–1511, doi:10.1175/JPO-D-12-0121.1, URL
554 <http://journals.ametsoc.org/doi/full/10.1175/JPO-D-12-0121.1>.

555 Chelton, D., and R. Deszoeke, 1998: Geographical variability of the first baroclinic Rossby
556 radius of deformation. *Journal of Physical Oceanography*, **28** (3), 433–460, doi:10.1175/
557 1520-0485(1998)028<0433:GVOTFB>2.0.CO;2, URL [http://journals.ametsoc.org/doi/abs/10.1175/1520-0485\(1998\)028<0433:GVOTFB>2.0.CO;2](http://journals.ametsoc.org/doi/abs/10.1175/1520-0485(1998)028<0433:GVOTFB>2.0.CO;2).

559 Chelton, D. B., M. G. Schlax, D. L. Witter, and J. G. Richman, 1990: Geosat Altimeter Observa-
560 tions of the Southern of the Surface Circulation. *Journal of Geophysical Research*, **95** (C10),
561 17 877–17 903.

562 Dee, D. P., and Coauthors, 2011: The ERA-Interim reanalysis: Configuration and perfor-
563 mance of the data assimilation system. *Quarterly Journal of the Royal Meteorological Society*,
564 **137** (April), 553–597, doi:10.1002/qj.828.

565 Dong, S., S. T. Gille, and J. Sprintall, 2007: An Assessment of the Southern Ocean Mixed Layer
566 Heat Budget. *Journal of Climate*, **20** (17), 4425–4442, doi:10.1175/JCLI4259.1, URL <http://journals.ametsoc.org/doi/abs/10.1175/JCLI4259.1>.

568 Dong, S., and K. A. Kelly, 2004: Heat Budget in the Gulf Stream Region: The Importance
569 of Heat Storage and Advection. *Journal of Physical Oceanography*, **34** (5), 1214–1231, doi:
570 10.1175/1520-0485(2004)034<1214:HBITGS>2.0.CO;2, URL <http://journals.ametsoc.org/doi/abs/10.1175/1520-0485\%282004\%29034\%3C1214\%3AHBITGS\%3E2.0.CO\%3B2>.

572 Dufour, C. O., L. L. Sommer, J. D. Zika, M. Gehlen, J. C. Orr, P. Mathiot, and B. Barnier,
573 2012: Standing and transient eddies in the response of the Southern Ocean meridional over-

- 574 turning to the Southern annular mode. *Journal of Climate*, **25** (20), 6958–6974, doi:10.1175/
575 JCLI-D-11-00309.1.
- 576 Faure, V., M. Arhan, S. Speich, and S. Gladyshev, 2011: Heat budget of the surface mixed layer
577 south of Africa. *Ocean Dynamics*, **61** (10), 1441–1458, doi:10.1007/s10236-011-0444-1, URL
578 <http://link.springer.com/10.1007/s10236-011-0444-1>.
- 579 Fenty, I., and P. Heimbach, 2013: Coupled Sea Ice-Ocean-State Estimation in the Labrador Sea
580 and Baffin Bay. *Journal of Physical Oceanography*, **43**, 884–904, doi:10.1175/JPO-D-12-065.
581 1, URL <http://journals.ametsoc.org/doi/abs/10.1175/JPO-D-12-065.1>.
- 582 Forget, G., 2010: Mapping Ocean Observations in a Dynamical Framework: A 2004–06 Ocean
583 Atlas. *Journal of Physical Oceanography*, **40** (6), 1201–1221, doi:10.1175/2009JPO4043.1,
584 URL <http://journals.ametsoc.org/doi/abs/10.1175/2009JPO4043.1>.
- 585 Gille, S., and K. Kelly, 1996: Scales of spatial and temporal variability in the Southern Ocean.
586 *Journal of Geophysical Research*, **101**, 8759–8773, URL <http://www.agu.org/pubs/crossref/1996/96JC00203.shtml>.
- 587 Hobbs, W. R., and M. N. Raphael, 2007: A representative time-series for the Southern Hemisphere
588 zonal wave 1. *Geophysical Research Letters*, **34**, 1–6, doi:10.1029/2006GL028740.
- 589 Hobbs, W. R., and M. N. Raphael, 2010: Characterizing the zonally asymmetric component of the
590 SH circulation. *Climate Dynamics*, **35**, 859–873, doi:10.1007/s00382-009-0663-z.
- 591 Ito, T., M. Woloszyn, and M. Mazloff, 2010: Anthropogenic carbon dioxide transport in the South-
592 ern Ocean driven by Ekman flow. *Nature*, **463** (7277), 80–83, doi:10.1038/nature08687, URL
593 <http://www.ncbi.nlm.nih.gov/pubmed/20054394>.

- 595 Iudicone, D., G. Madec, and T. J. McDougall, 2008: Water-mass transformations in a neu-
596 tral density framework and the key role of light penetration. *Journal of Physical Oceanogra-*
597 *phy*, **38** (7), 1357–1376, doi:10.1175/2007JPO3464.1, URL <http://ams.allenpress.com/perlserv/?request=get-document&doi=10.1175/2007JPO3464.1>.
- 598
- 599 Jerlov, N. G., 1968: *Optical Oceanography*. Elsevier, 199 pp.
- 600 Karsten, R. H., and J. Marshall, 2002: Constructing the Residual Circulation of the ACC
601 from Observations. *Journal of Physical Oceanography*, **32** (1951), 3315–3327, doi:10.1175/
602 1520-0485(2002)032<3315:CTRCOT>2.0.CO;2.
- 603 Large, W. G., J. C. McWilliams, and S. C. Doney, 1994: Oceanic vertical mixing: A review
604 and a model with a nonlocal boundary layer parameterization. *Reviews of Geophysics*, doi:
605 10.1029/94RG01872.
- 606 Large, W. G., and S. G. Yeager, 2009: The global climatology of an interannually varying air-
607 sea flux data set. *Climate Dynamics*, **33** (2-3), 341–364, doi:10.1007/s00382-008-0441-3, URL
608 <http://link.springer.com/10.1007/s00382-008-0441-3>.
- 609 Lenn, Y.-D., and T. K. Chereskin, 2009: Observations of Ekman Currents in the Southern Ocean.
610 *Journal of Physical Oceanography*, **39** (3), 768–779, doi:10.1175/2008JPO3943.1.
- 611 Marshall, J., A. Adcroft, C. Hill, L. Perelman, and C. Heisey, 1997: A finite-volume, incompress-
612 ible Navier Stokes model for studies of the ocean on parallel computers. *Journal of Geophysical
613 Research*, **102** (C3), 5753–5766.
- 614 Marshall, J., and T. Radko, 2003: Residual-Mean Solutions for the Antarctic Circumpolar Current
615 and Its Associated Overturning Circulation. *Journal of Physical Oceanography*, **33**, 2341–2354,
616 doi:10.1175/1520-0485(2003)033<2341:RSFTAC>2.0.CO;2.

- 617 Mazloff, M. R., P. Heimbach, and C. Wunsch, 2010: An Eddy-Permitting Southern Ocean State
618 Estimate. *Journal of Physical Oceanography*, **40** (5), 880–899, doi:10.1175/2009JPO4236.1,
619 URL <http://journals.ametsoc.org/doi/abs/10.1175/2009JPO4236.1>.
- 620 Milliff, R. F., T. J. Hoar, H. van Loon, and M. Raphael, 1999: Quasi-stationary wave variability in
621 NSCAT winds. *Journal of Geophysical Research*, **104**, 11 425, doi:10.1029/1998JC900087.
- 622 Morrison, A. K., A. M. Hogg, and M. L. Ward, 2011: Sensitivity of the Southern Ocean over-
623 turning circulation to surface buoyancy forcing. *Geophysical Research Letters*, **38** (May), 1–5,
624 doi:10.1029/2011GL048031.
- 625 Morrison, A. K., O. A. Saenko, A. M. Hogg, and P. Spence, 2013: The role of vertical eddy
626 flux in Southern Ocean heat uptake. *Geophysical Research Letters*, **40** (20), 5445–5450, doi:
627 10.1002/2013GL057706.
- 628 Naveira Garabato, A. C., R. Ferrari, and K. L. Polzin, 2011: Eddy stirring in the Southern Ocean.
629 *Journal of Geophysical Research*, **116** (C9), C09019, doi:10.1029/2010JC006818, URL <http://doi.wiley.com/10.1029/2010JC006818>.
- 631 O'Neill, L. W., D. B. Chelton, and S. K. Esbensen, 2003: Observations of SST-induced pertur-
632 bations of the wind stress field over the Southern Ocean on seasonal timescales. *Journal of*
633 *Climate*, **16**, 2340–2354, doi:10.1175/2780.1.
- 634 O'Neill, L. W., D. B. Chelton, S. K. Esbensen, and F. J. Wentz, 2005: High-resolution satellite
635 measurements of the atmospheric boundary layer response to SST variations along the Agulhas
636 Return Current. *Journal of Climate*, **18**, 2706–2723, doi:10.1175/JCLI3415.1.

- 637 Paulson, C. A., and J. J. Simpson, 1977: Irradiance Measurements in the Upper Ocean. *Journal*
638 *of Physical Oceanography*, **7**, 952–956, doi:10.1175/1520-0485(1977)007<0952:IMITUO>2.
639 0.CO;2.
- 640 Radko, T., and J. C. Marshall, 2006: The Antarctic Circumpolar Current in Three Dimensions.
641 *Journal of Physical Oceanography*, **36**, 651–669, doi:10.1175/JPO2893.1.
- 642 Rintoul, S. R., and M. H. England, 2002: Ekman Transport Dominates Local Air-Sea Fluxes in
643 Driving Variability of Subantarctic Mode Water. *Journal of Physical Oceanography*, **32** (5),
644 1308–1321.
- 645 Rocha, C. B., T. K. Chereskin, S. T. Gille, and D. Menemenlis, 2015: Mesoscale to submesoscale
646 wavenumber spectra in Drake Passage. *Journal of Physical Oceanography*, 1–17, doi:10.1175/
647 JPO-D-15-0087.1.
- 648 Roemmich, D., J. Gilson, J. Willis, P. Sutton, and K. Ridgway, 2005: Closing the time-varying
649 mass and heat budgets for large ocean areas: The Tasman Box. *Journal of Climate*, **18**, 2330–
650 2343, doi:10.1175/JCLI3409.1.
- 651 Sallée, J.-B., R. Morrow, and K. Speer, 2008: Eddy heat diffusion and Subantarctic Mode Water
652 formation. *Geophysical Research Letters*, **35** (5), L05 607, doi:10.1029/2007GL032827, URL
653 <http://doi.wiley.com/10.1029/2007GL032827>.
- 654 Sallée, J.-B., K. Speer, R. Morrow, and N. Wienders, 2006: Formation of subantarctic mode
655 water in the southeastern Indian Ocean. *Ocean Dynamics*, **56** (5-6), 525–542, doi:10.1007/
656 s10236-005-0054-x, URL <http://link.springer.com/10.1007/s10236-005-0054-x>.

- 657 Sallée, J. B., K. G. Speer, and S. R. Rintoul, 2010: Zonally asymmetric response of the Southern
658 Ocean mixed-layer depth to the Southern Annular Mode. *Nature Geoscience*, **3** (4), 273–279,
659 doi:10.1038/ngeo812, URL <http://dx.doi.org/10.1038/ngeo812>.
- 660 Sarmiento, J. L., N. Gruber, M. A. Brzezinski, and J. P. Dunne, 2004: High-latitude controls of
661 thermocline nutrients and low latitude biological productivity. *Nature*, **427** (January), 56–60,
662 doi:10.1038/nature10605.
- 663 Sloyan, B. M., and S. R. Rintoul, 2001: Circulation, Renewal, and Modification of Antarctic
664 Mode and Intermediate Water*. *Journal of Physical Oceanography*, **31** (4), 1005–1030, doi:
665 10.1175/1520-0485(2001)031<1005:CRAMOA>2.0.CO;2.
- 666 Sokolov, S., and S. R. Rintoul, 2009: Circumpolar structure and distribution of the antarc-
667 tic circumpolar current fronts: 2. Variability and relationship to sea surface height. *Jour-
668 nal of Geophysical Research: Oceans*, **114**, C11 019, doi:10.1029/2008JC005248, URL <http://doi.wiley.com/10.1029/2008JC005248>.
- 670 Speer, K., S. R. Rintoul, and B. Sloyan, 2000: The Diabatic Deacon Cell*. *Journal of Physical
671 Oceanography*, **30**, 3212–3222, doi:10.1175/1520-0485(2000)030<3212:TDDC>2.0.CO;2.
- 672 Sun, C., and D. R. Watts, 2002: Heat flux carried by the Antarctic Circumpolar Current mean
673 flow. *Journal of Geophysical Research*, **107** (C9), 3119, doi:10.1029/2001JC001187, URL <http://doi.wiley.com/10.1029/2001JC001187>.
- 675 Thompson, A. F., and J.-B. Sallee, 2012: Jets and topography: jet transitions and the im-
676 pact on transport in the Antarctic Circumpolar Current. *Journal of Physical Oceanogra-
677 phy*, **42**, 956–973, doi:10.1175/JPO-D-11-0135.1, URL <http://journals.ametsoc.org/doi/pdf/10.1175/JPO-D-11-0135.1>.

- van Loon, H., and R. L. Jenne, 1972: The zonal harmonic standing waves in the southern hemisphere. *Journal of Geophysical Research*, **77** (6), 992, doi:10.1029/JC077i006p00992.
- Vivier, F., D. Iudicone, F. Busdraghi, and Y.-H. Park, 2009: Dynamics of sea-surface temperature anomalies in the Southern Ocean diagnosed from a 2D mixed-layer model. *Climate Dynamics*, **34** (2-3), 153–184, doi:10.1007/s00382-009-0724-3, URL <http://link.springer.com/10.1007/s00382-009-0724-3>.
- Vivier, F., K. A. Kelly, and L. A. Thompson, 2002: Heat Budget in the Kuroshio Extension Region: 1993-99. *Journal of Physical Oceanography*, **32** (12), 3436–3454, doi:10.1175/1520-0485(2002)032<3436:HBITKE>2.0.CO;2, URL <http://journals.ametsoc.org/doi/abs/10.1175/1520-0485\%282002\%29032\%3C3436\%3AHBITKE\%3E2.0.CO\%3B2>.
- Wang, J., M. R. Mazloff, and S. T. Gille, 2014: Pathways of the Agulhas waters poleward of 29S. *Journal of Geophysical Research : Oceans*, **119**, 4234–4250, doi:10.1002/jgrc.20224.
- Wolfe, C. L., P. Cessi, J. L. McClean, and M. E. Maltrud, 2008: Vertical heat transport in eddying ocean models. *Geophysical Research Letters*, **35** (23), 1–5, doi:10.1029/2008GL036138.
- Wunsch, C., and P. Heimbach, 2013: Dynamically and kinematically consistent global ocean circulation and ice state estimates. *International Geophysics*, **103**, 553–579, doi:10.1016/B978-0-12-391851-2.00021-0.
- Yu, L., and R. A. Weller, 2007: Objectively analyzed air-sea heat fluxes for the global ice-free oceans (1981-2005). *Bulletin of the American Meteorological Society*, **88** (April), 527–539, doi:10.1175/BAMS-88-4-527.

699 **LIST OF TABLES**

700 Table 1.	SOSE 2005-2010 mean heat budget terms from equation (1) in PW integrated	
701 over the upper 624 m and between SSH lines as described in section 2 for the		
702 entire ACC and the Atlantic/Indian and Pacific sectors separately.		34

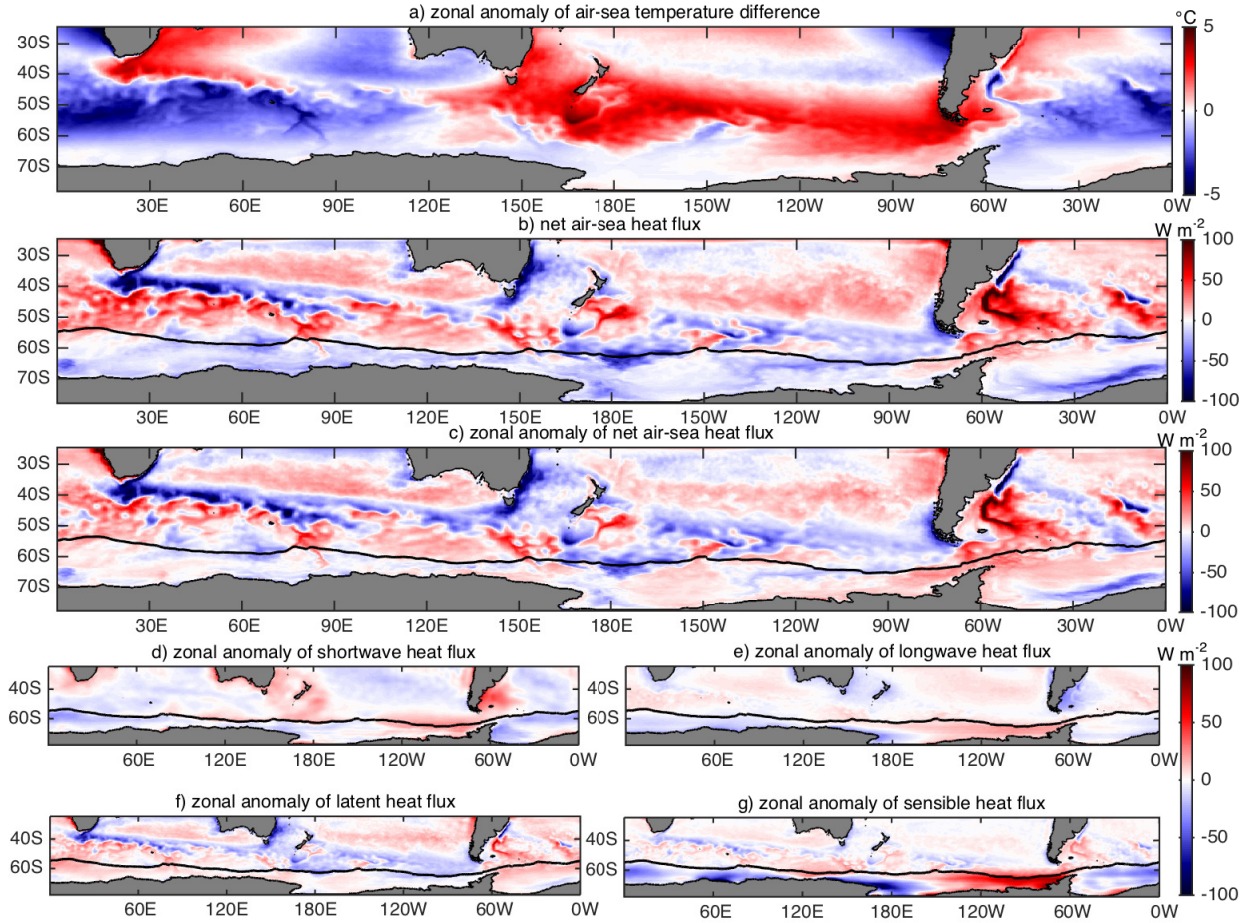
703 TABLE 1. SOSE 2005-2010 mean heat budget terms from equation (1) in PW integrated over the upper 624 m
 704 and between SSH lines as described in section 2 for the entire ACC and the Atlantic/Indian and Pacific sectors
 705 separately.

Heat budget term (PW)	Total	Atlantic/Indian	Pacific
air-sea flux	0.27	0.35	-0.08
geostrophic advection	0.38	0.13	0.25
<i>mean</i>	0.23	-0.01	0.24
<i>eddy</i>	0.15	0.14	0.01
ageostrophic advection	-0.58	-0.42	-0.16
vertical advection	-0.09	-0.06	-0.03
<i>mean</i>	-0.23	-0.18	-0.05
<i>eddy</i>	0.14	0.12	0.02
diffusion	0	0	0
temperature tendency	-0.02	0.00	-0.02

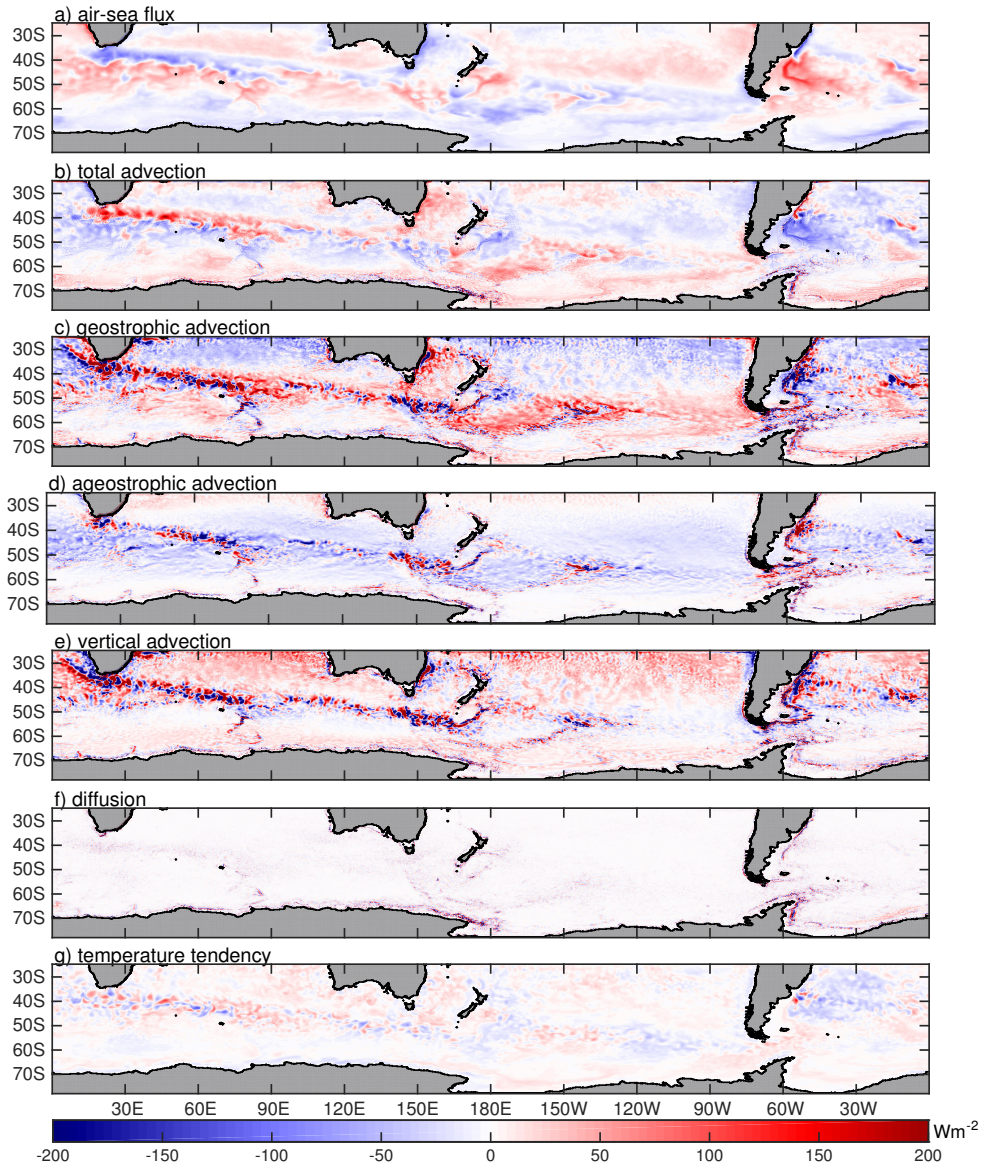
706 LIST OF FIGURES

- 707 **Fig. 1.** SOSE 2005-2010 mean of a) zonal anomaly of sea surface temperature ($^{\circ}\text{C}$), b) net air-
 708 sea heat flux (W m^{-2}) with positive defined as heat flux into the ocean, c) zonal anomaly
 709 of net air-sea heat flux, d) zonal anomaly of net shortwave heat flux, e) zonal anomaly of
 710 net longwave radiation (incoming-outgoing) f) zonal anomaly of net latent heat flux and g)
 711 zonal anomaly net sensible heat flux. We focus on flux patterns north of the 2005-2010
 712 annual mean sea ice boundary (black contour). 37
- 713 **Fig. 2.** SOSE 2005-2010 mean heat budget terms from equation 1, integrated over the upper 624 m
 714 in W m^{-2} . Total divergence of temperature advection b) is the sum of the total geostrophic
 715 horizontal c), ageostrophic horizontal d) and vertical e) components of advection. Positive
 716 (red) is warming and negative (blue) is cooling. 38
- 717 **Fig. 3.** Similar to Figure 2 but for the time-mean and eddy components of horizontal geostrophic
 718 and vertical advection. The topographic features labelled on panel d) are from left to right:
 719 Kerguelen Plateau (KP), Macquarie Ridge (MR), Campbell Plateau (CP), Pacific-Antarctic
 720 Ridge (PAR) and Drake Passage (DP). Units are W m^{-2} 39
- 721 **Fig. 4.** SOSE vertically and meridionally integrated heat budget solution: a) 2005-2010 mean net
 722 air-sea heat flux (colors) with SSH contours defining the northern and southern integration
 723 boundaries (solid lines), b) heat budget terms in equation 1 integrated to 624 m and be-
 724 tween SSH contours (Wm^{-1}) and c) cumulative sum of the terms in b) in PW as well as
 725 the mean temperature averaged vertically in the upper ocean (to 624 m) and between SSH
 726 contours in a) (black dashed line) and d) cumulative sum of mean and eddy contributions
 727 to the geostrophic and vertical advection terms (PW). Grey dashed lines mark Campbell
 728 Plateau and Drake Passage, separating the Atlantic/Indian sector from the Pacific sector.
 729 Total integrated values are listed in Table 1. 40
- 730 **Fig. 5.** Cumulatively summed heat budget terms as in Figure 4 with each season separately, with the
 731 terms in equation 1 in the left panels and the time-mean and eddy components of geostrophic
 732 and vertical advection in the right panels: a) and b) March, April, May (MAM), c) and d)
 733 June, July, August (JJA), e) and f) September, October, November (SON), and g) and h)
 734 December, January, February (DJF). Note that the y axis limits in the left panels differ for
 735 each season to capture the large seasonal cycle in air-sea fluxes. All units are in PW. 41
- 736 **Fig. 6.** Time series of seasonal (3-month) integrated heat budget terms in Wm^{-2} (left) and time-mean
 737 terms (right) with error bars indicating one standard deviation above and below the mean for
 738 a) average of the Atlantic/Indian sector of the ACC, b) average of the Pacific sector of the
 739 ACC, and c) difference between a) and b). 42
- 740 **Fig. 7.** Integrated heat budget terms similar to Figure 4 for the Agulhas Return Current (ARC)
 741 cooling region: a) air-sea heat flux in the ARC region; black lines show the sea surface
 742 height contour used as the southern boundary and a line of constant latitude used as the
 743 northern boundary to integrate the heat budget terms in equation 1; b) heat budget terms in
 744 equation 1 integrated to 624 m and between meridional contours shown in a) (Wm^{-1}); c)
 745 cumulative sum of heat budget terms integrated to 624 m and between bounds in a); and d)
 746 cumulative sum of mean and eddy contributions to the geostrophic and vertical advection
 747 terms. 43
- 748 **Fig. A1.** Comparison between Ekman transport calculated from SOSE wind stress fields and
 749 ageostrophic transport calculated from the residual between total and geostrophic velocities

750 integrated vertically over the Ekman layer. a) zonal Ekman transport, b) zonal ageostrophic
751 transport, c) meridional Ekman transport, and d) meridional ageostrophic transport. 44



752 FIG. 1. SOSE 2005-2010 mean of a) zonal anomaly of sea surface temperature ($^{\circ}\text{C}$), b) net air-sea heat flux
 753 (W m^{-2}) with positive defined as heat flux into the ocean, c) zonal anomaly of net air-sea heat flux, d) zonal
 754 anomaly of net shortwave heat flux, e) zonal anomaly of net longwave radiation (incoming-outgoing) f) zonal
 755 anomaly of net latent heat flux and g) zonal anomaly net sensible heat flux. We focus on flux patterns north of
 756 the 2005-2010 annual mean sea ice boundary (black contour).



757 FIG. 2. SOSE 2005-2010 mean heat budget terms from equation 1, integrated over the upper 624 m in W
 758 m^{-2} . Total divergence of temperature advection b) is the sum of the total geostrophic horizontal c), ageostrophic
 759 horizontal d) and vertical e) components of advection. Positive (red) is warming and negative (blue) is cooling.

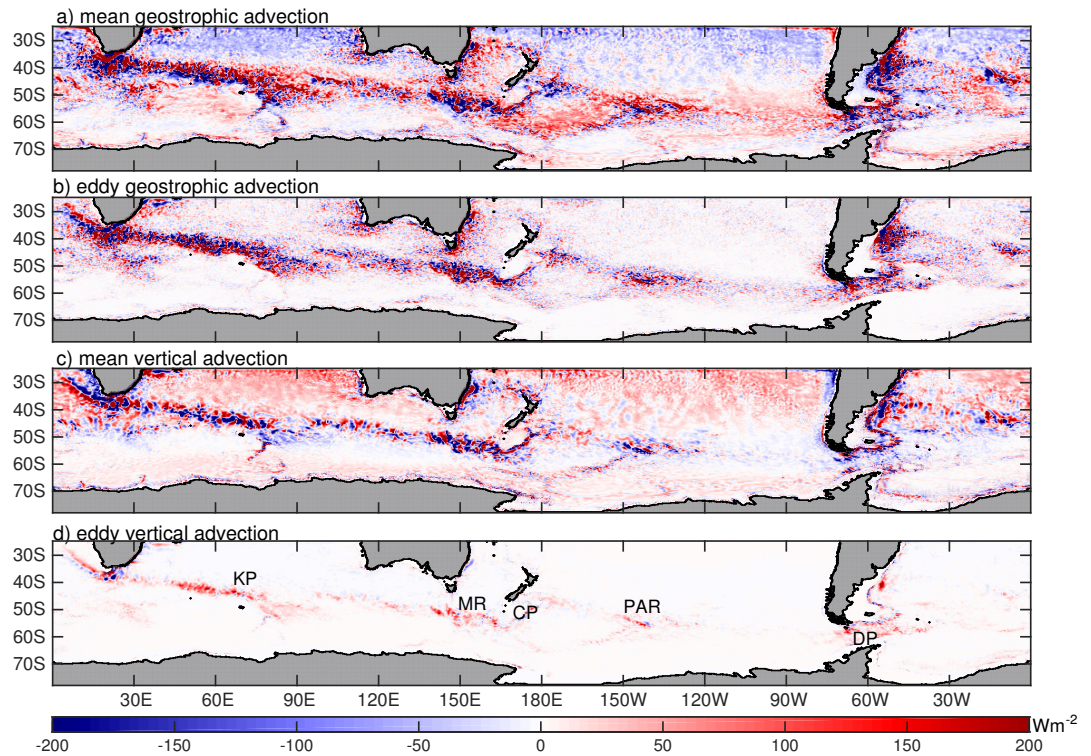
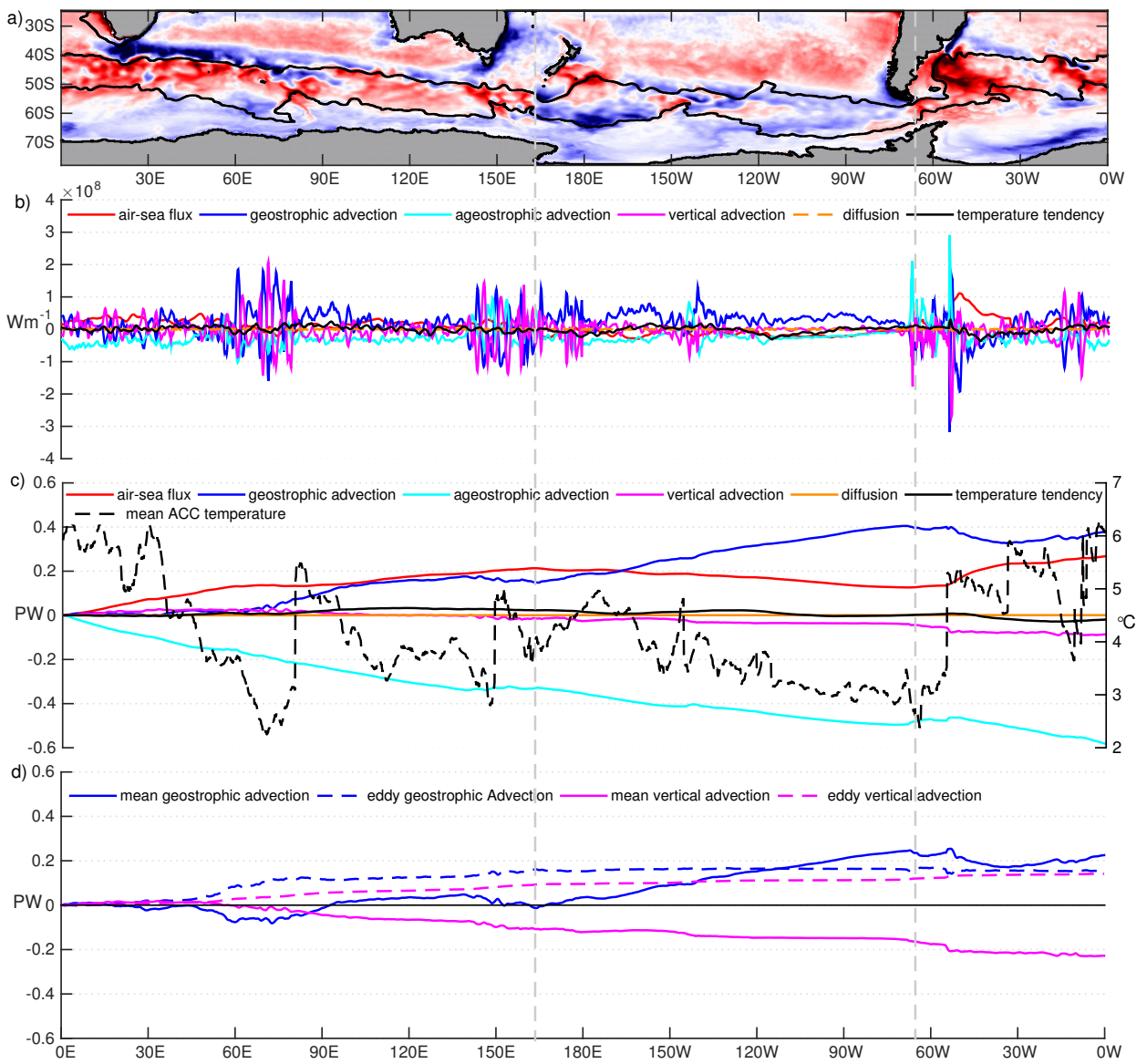
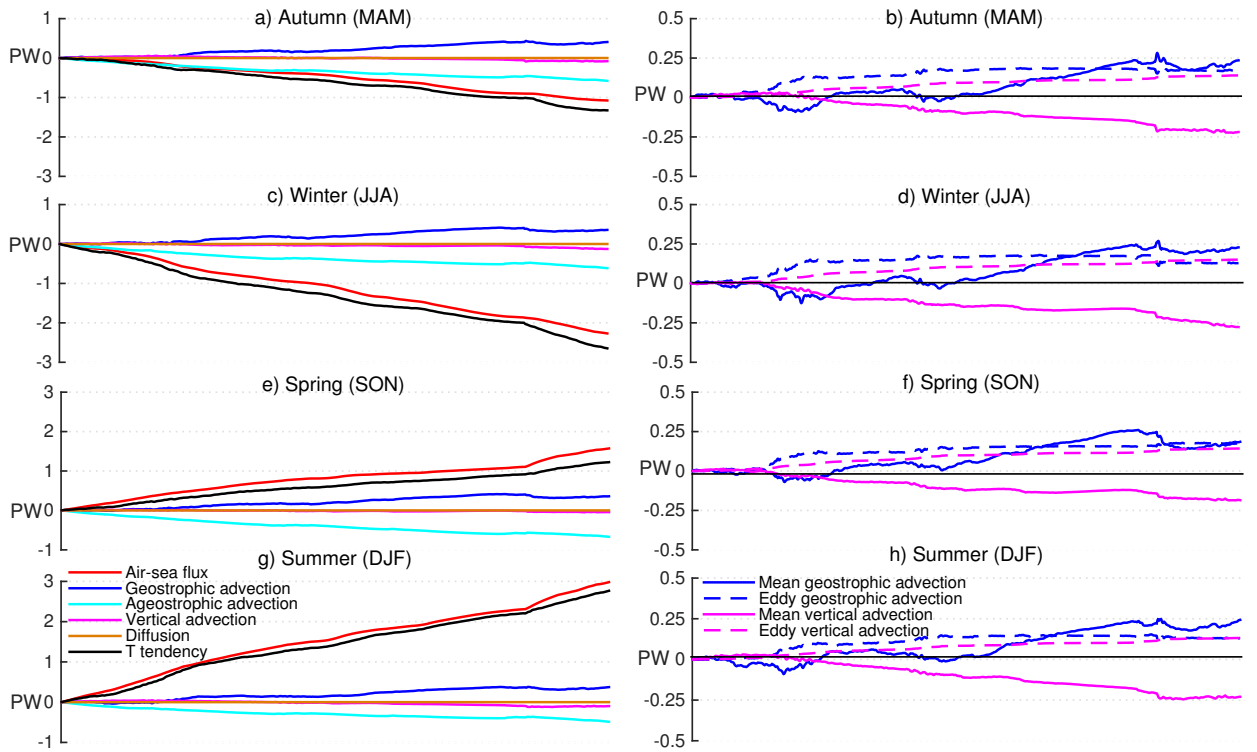


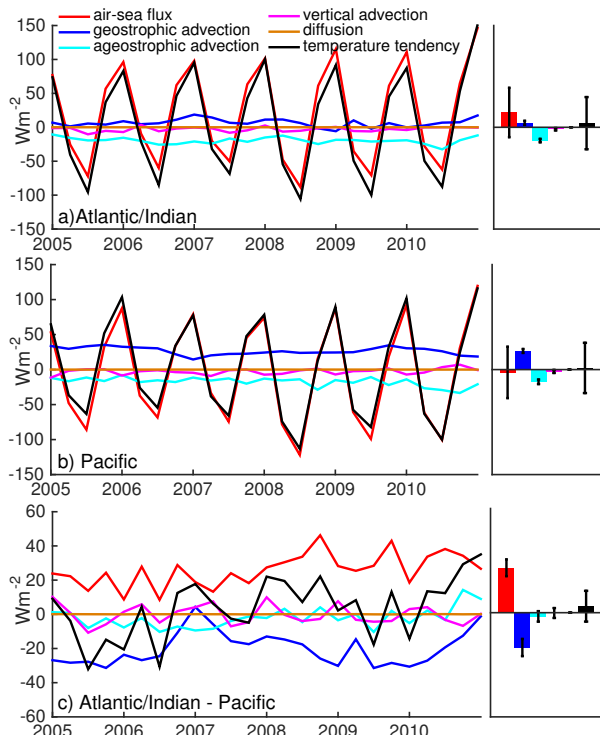
FIG. 3. Similar to Figure 2 but for the time-mean and eddy components of horizontal geostrophic and vertical advection. The topographic features labelled on panel d) are from left to right: Kerguelen Plateau (KP), Macquarie Ridge (MR), Campbell Plateau (CP), Pacific-Antarctic Ridge (PAR) and Drake Passage (DP). Units are Wm^{-2} .



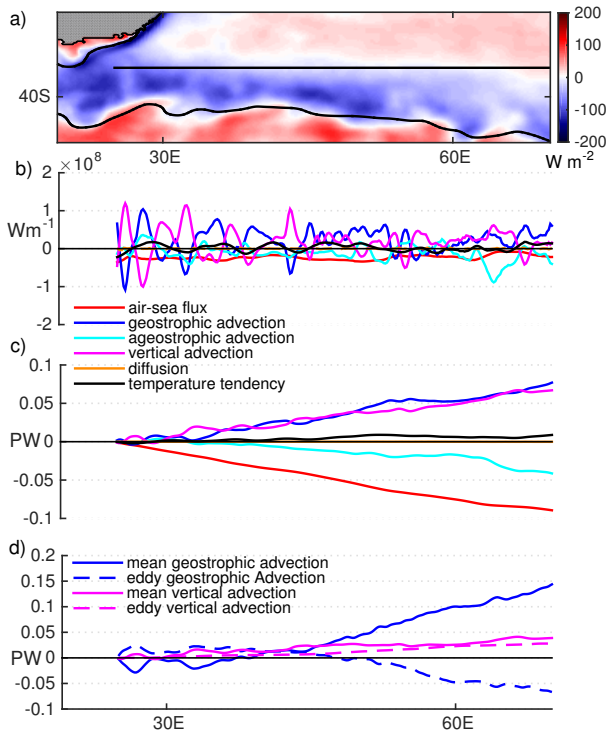
764 FIG. 4. SOSE vertically and meridionally integrated heat budget solution: a) 2005-2010 mean net air-sea heat
 765 flux (colors) with SSH contours defining the northern and southern integration boundaries (solid lines), b) heat
 766 budget terms in equation 1 integrated to 624 m and between SSH contours (Wm^{-1}) and c) cumulative sum of
 767 the terms in b) in PW as well as the mean temperature averaged vertically in the upper ocean (to 624 m) and
 768 between SSH contours in a) (black dashed line) and d) cumulative sum of mean and eddy contributions to the
 769 geostrophic and vertical advection terms (PW). Grey dashed lines mark Campbell Plateau and Drake Passage,
 770 separating the Atlantic/Indian sector from the Pacific sector. Total integrated values are listed in Table 1.



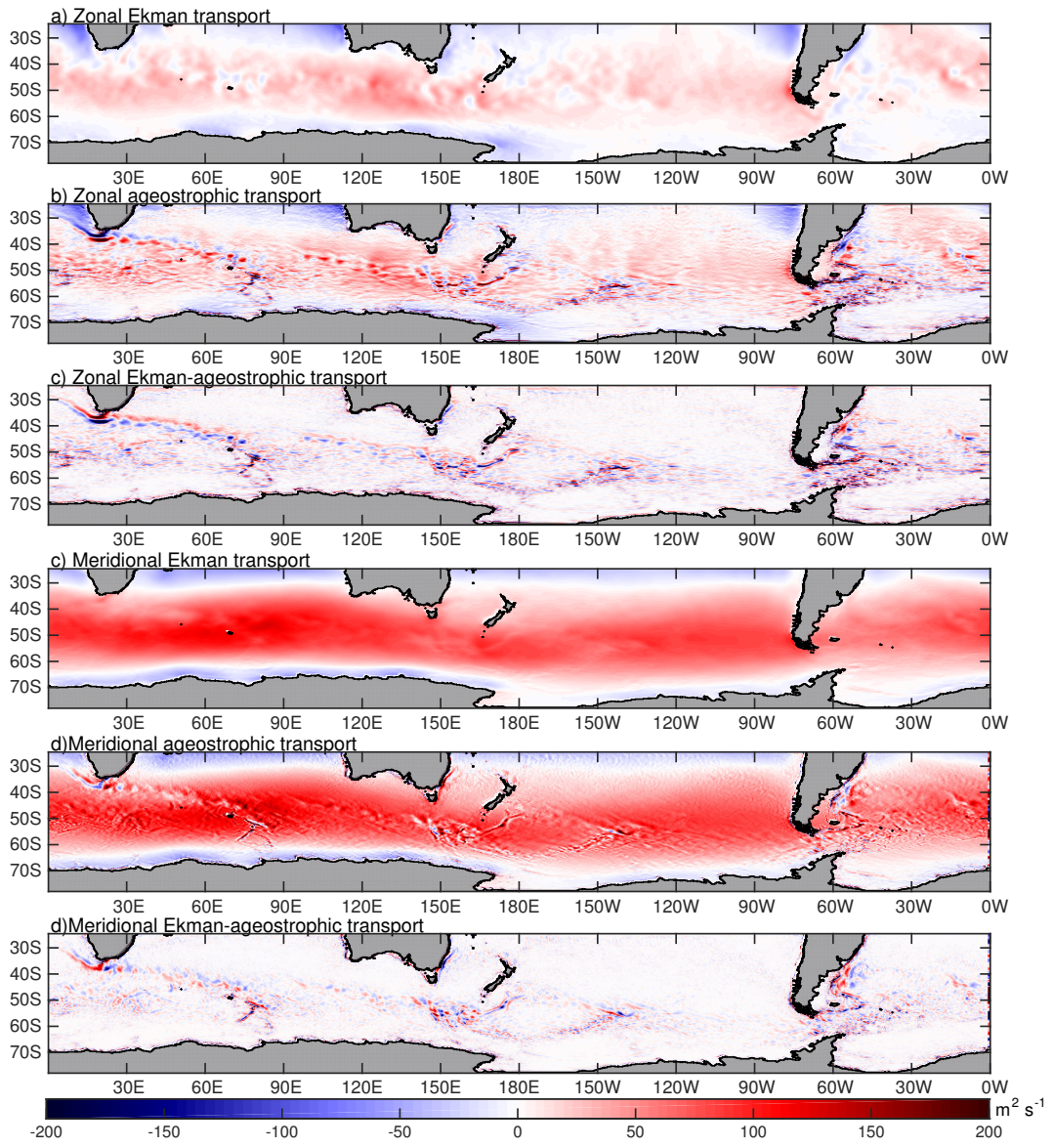
771 FIG. 5. Cumulatively summed heat budget terms as in Figure 4 with each season separately, with the terms in
 772 equation 1 in the left panels and the time-mean and eddy components of geostrophic and vertical advection in
 773 the right panels: a) and b) March, April, May (MAM), c) and d) June, July, August (JJA), e) and f) September,
 774 October, November (SON), and g) and h) December, January, February (DJF). Note that the y axis limits in the
 775 left panels differ for each season to capture the large seasonal cycle in air-sea fluxes. All units are in PW.



776 FIG. 6. Time series of seasonal (3-month) integrated heat budget terms in Wm^{-2} (left) and time-mean terms
 777 (right) with error bars indicating one standard deviation above and below the mean for a) average of the At-
 778 lantic/Indian sector of the ACC, b) average of the Pacific sector of the ACC, and c) difference between a) and
 779 b).



780 FIG. 7. Integrated heat budget terms similar to Figure 4 for the Agulhas Return Current (ARC) cooling
 781 region: a) air-sea heat flux in the ARC region; black lines show the sea surface height contour used as the
 782 southern boundary and a line of constant latitude used as the northern boundary to integrate the heat budget
 783 terms in equation 1; b) heat budget terms in equation 1 integrated to 624 m and between meridional contours
 784 shown in a) (W m^{-1}); c) cumulative sum of heat budget terms integrated to 624 m and between bounds in a); and
 785 d) cumulative sum of mean and eddy contributions to the geostrophic and vertical advection terms.



786 Fig. A1. Comparison between Ekman transport calculated from SOSE wind stress fields and ageostrophic
 787 transport calculated from the residual between total and geostrophic velocities integrated vertically over the
 788 Ekman layer. a) zonal Ekman transport, b) zonal ageostrophic transport, c) meridional Ekman transport, and d)
 789 meridional ageostrophic transport.